

UC Berkeley

Controls and Information Technology

Title

Measuring 3D indoor air velocity via an inexpensive low-power ultrasonic anemometer

Permalink

<https://escholarship.org/uc/item/43c525tg>

Authors

Arens, Edward
Ghahramani, Ali
Przybyla, Richard
[et al.](#)

Publication Date

2020-03-01

DOI

10.1016/j.enbuild.2020.109805

License

<https://creativecommons.org/licenses/by-nc-sa/4.0/> 4.0

Peer reviewed

Measuring 3D indoor air velocity via an inexpensive low-power ultrasonic anemometer

Edward Arens^{1*}, Ali Ghahramani¹, Richard Przybyla², Michael Andersen³, Syung Min⁴, Therese Peffer¹, Paul Raftery¹, Megan Zhu⁵, Vy Luu⁴, Hui Zhang¹

¹ Center for the Built Environment, University of California, Berkeley, 390 Wurster Hall, Berkeley, CA 94720

² Chirp Microsystems, Berkeley CA

³ Department of Electrical Engineering and Computer Science, UC Berkeley,

⁴ Department of Mechanical Engineering, UC Berkeley

⁵ College of Letters and Science, UC Berkeley

*Corresponding author: earens@berkeley.edu

Abstract

The ability to inexpensively monitor indoor air speed and direction on a continuous basis would transform the control of environmental quality and energy use in buildings. Air motion transports energy, ventilation air, and pollutants around building interiors and their occupants, and measured feedback about it could be used in numerous ways to improve building operation. However indoor air movement is rarely monitored because of the expense and fragility of sensors. This paper describes a unique anemometer developed by the authors, that measures 3-dimensional air velocity for indoor environmental applications, leveraging new microelectromechanical systems (MEMS) technology for ultrasonic range-finding. The anemometer uses a tetrahedral arrangement of four transceivers, the smallest number able to capture a 3-dimensional flow, that provides greater measurement redundancy than in existing anemometry. We describe the theory, hardware, and software of the anemometer, including algorithms that detect and eliminate shielding errors caused by the wakes from anemometer support struts. The anemometer has a resolution and starting threshold of 0.01m/s, an absolute air speed error of 0.05 m/s at a given orientation with minimal filtering, 3.1° angle- and 0.11m/s velocity errors over 360° azimuthal rotation, and 3.5° angle- and 0.07m/s velocity errors over 135° vertical declination. It includes radio connection to internet and is able to operate standalone for multiple years on a standard battery. The anemometer also measures temperature and has a compass and tilt sensor so that flow direction is globally referenced regardless of anemometer orientation. The retail cost of parts is \$100 USD, and all parts snap together for ease of assembly.

Keywords: 3-dimensional air velocity monitoring, indoor anemometer, tetrahedron, ultrasonic anemometry; ultrasonic pulse time of flight; MEMS ultrasound; sonic temperature

Introduction

Measuring indoor air movement

There are many reasons for measuring and managing air movement in indoor spaces. Air movement cooling is an efficient way to provide occupants comfort and to relieve physiological heat stress [1]. It can conversely be excessive at low temperatures, causing the perception of draft. Fresh air ventilation in the breathing zone affects comfort, health, and productivity, and, in some occupancies, health and safety through the dispersal of pollutants or pathogens. The operation of building air movement systems, such as natural ventilation supply, operable windows, and ceiling fans, would ideally be based on measured feedback about the air movement occurring in the space, rather than on conservative assumptions made at the time of their design. Similarly, the escape of airborne disease vectors from isolation zones in hospitals, smoke movement, or transport of harmful gases or particulates in labs, cleanrooms, and factories, could be detected and quantified by monitoring indoor airflow direction and speed, affecting the amount of pressurization now needed to assure safe operation of such buildings. Finally, most offices, labs, hospitals, and data centers in the U.S. use air-systems to transport warmth and coolth, and energy management systems would benefit from knowledge of airborne energy flows within such indoor spaces.

There are complex relationships between air movement and the energy used for comfort and ventilation. Ref [2] summarizes these, and the role of measurement, for the operation of variable-air-volume systems, the most prevalent HVAC system in large buildings. The room air speeds required in such systems are low, below 0.2 m/s, which are not easy to measure. At the same time, the building profession has recently become aware that occupants commonly prefer elevated air movement [3,4], and that cooling occupants directly with room air movement in the range of 0.3 to 1.5 m/s can enable major HVAC energy efficiencies [5] while providing a wider range of comfortable conditions in a space [6]. Refs [7,8] summarize these effects and provide recent results about integrating the room airflow patterns from ceiling fans into the design of comfortable and energy-efficient work spaces. Because airflow patterns are non-uniform and complex, there are opportunities for sensing and feedback in their control.

At present, airflow within rooms is rarely measured, and its monitoring over time is virtually nonexistent. This has been due to the expense, power draw, directional sensitivity, calibration drift, and fragility of existing anemometers. Air movement is instead approximated from sensors in the rooms' supply and return ducts, whose high flow rates are easier to measure, but which only indirectly represent the actual flows in the rooms.

An instrument appropriate for measuring air speed in indoor spaces should have a low minimum (starting) speed (below 0.05m/s; 10fpm), and be precise for the low speeds that predominate indoors (particularly below 1m/s). There is rarely need to measure speeds above 10 or even 5m/s. There are also applications requiring the *direction* of the air movement. Fire/smoke/pathogen alarms require knowing the direction more so than the speed. Along with these, controllers for ceiling fans, natural ventilation devices, and systems creating thermal stratification in spaces would each benefit from knowing the three-dimensional air speed vector and its vertical and lateral velocity components. A portable anemometer taking such directional airflow measurements would preferably also measure its own orientation to assure that its measurements are globally correct, since instruments in buildings are prone to become shifted for various reasons.

Finally, the ability to *monitor over time* the airstream of interest, with wireless connectivity and low energy (long life operating standalone on battery), would have great value. The analog for such monitoring would be the self-contained temperature loggers/transmitters that in recent decades have transformed building monitoring for research, evaluation, and ultimately control. Battery-powered long-term monitoring capability does not currently exist for indoor air movement. It would be useful both for

research projects and for controlling the building systems that affect the air movement in buildings. A related monitoring application is ‘desktop weather stations’ that integrate air speed measurement together with other environmental parameters to continuously evaluate thermal comfort and indoor environmental quality [9–11].

Currently, most indoor air flows are measured by various types of heated-element anemometers [12–18]. Although they are capable of being calibrated to measure low speeds and indoor turbulence levels [17], they are limited by the need to overheat the sensing element(s). This requires more power than is possible for lengthy standalone battery-powered operation, requires fragile or foulable elements, and generates buoyant convection around the element that influences the lowest-speed measurements. Handheld versions tend to measure only a narrow range of flow directions, since the heated element must be surrounded by a protective cowling [14]. Omnidirectional (heated sphere on a stalk) versions [15–17] are insensitive to flow direction, which makes them suitable for evaluating occupant comfort, but because they are fragile they have mostly been used in research applications. There has been recent development of heated-element arrays manufactured through MEMS (microelectromechanical systems) techniques, capable of detecting air flow speed and direction in two-dimensions [19]. This is promising because the thermal power requirements of an anemometer using such an element are potentially low. At this point we are not aware of an anemometer using such technology.

Measurement or monitoring of *three-dimensional* air speed vectors is very uncommon for indoor applications. The traditional instrument capable of such measurements uses orthogonally crossed-hotwires [18], used in aerodynamics research laboratories, with extreme fragility (and highest sensitivity). In addition, there are ultrasonic anemometers that measure directional velocities using three pairs of transducers sending and receiving sonic pulses. A very few such devices are marketed for indoor airflow measurement in cleanrooms [20], and they have been very expensive due to their analog acoustical electronics. The primary use of 3D ultrasonics is outdoors, in large instruments used by weather services (they are durable with no moving parts), and in micrometeorological research on turbulent fluxes of momentum, heat, moisture, and pollutants in the atmospheric boundary layer [21]. Several such devices are commercially available, and there is a substantial literature evaluating their performance and devising compensation for airflow distortion (termed ‘shielding’ or ‘shadowing’) errors induced by their aerodynamic shapes [22–25].

Opportunity:

Very recently there have emerged ultrasonic speakers/microphones made using MEMS manufacturing techniques. Such devices are integrated with their processors as single chips on silicon wafers, so that communications are digital. They are very small and are potentially very inexpensive. Their initial applications have been in computer-game range-finding, but they could also be applied to measuring air movement. They operate at very high ultrasonic frequencies, which opens the opportunity for lower velocity thresholds, higher sensitivity at low speeds, minimizing size of anemometer, including multiple directional axes, low power consumption, long monitoring life, and mass production.

The Chirp Microsystems CH-101 transceiver was developed over the last five years. ‘Transceiver’ signifies transmitter, receiver, and digital processing of signals. It combines the functions of actuator (speaker), sensor (microphone), signal processing and communication, all of which are integrated within the silicon wafer for mass fabrication. The signaling is via pulses, and the vibration frequency within the pulses is approximately 175kHz. The frequency of transmission in current ultrasonic anemometers is typically 40kHz.

We set a goal to use this device to build an anemometer with a lower threshold comparable to the best existing anemometry used in indoor applications (<0.05m/s, 10fpm). The upper speed capability was less

critical, ideally 10 m/s, but few current indoor applications involve air speeds reaching this level. The size of the instrument needed to be comparable to existing indoor sensing devices, much smaller than current outdoor ultrasonic anemometers.

The natural frequency and responsiveness of ultrasonic transceiver membranes affect the dimensions possible for the anemometer: shorter distances between transceivers allow higher speed measurements, but reduce the accuracy at lower speeds. Reducing the frequency of the transceiver membranes also allows higher speeds, again at the cost of low-end accuracy. Lower frequencies extend the measuring distance possible between transceivers, but increasing the size of an indoor anemometer is generally not desirable. Using 175 kHz to measure the above velocity ranges results in a measurement volume that is sized somewhere between that of a tennis ball and a golf ball. This is an appropriate size for measuring most effects related to human and building scales.

To reach our low-cost objective, we developed an anemometer configuration that measures three-dimensional flow using only four transceivers, instead of six as in presently available anemometers. This configuration also confers some unique and significant advantages in improving the anemometer's accuracy.

Finally, the low power requirements of the transceivers' pulses makes possible long-term (years' scale) standalone operation on a battery, even with continuous radio/internet communication.

Objective

This paper intends to describe the new anemometer concept and its development—the challenges and solutions devised, as well as its performance characteristics and validation. We hope that, given a clear understanding of the anemometer's capabilities, the building professions (and manufacturers) will be able to formulate new ways to use enhanced air flow measurement for their specific applications related to the indoor environment.

Description of anemometer

The anemometer involves both new hardware and software. These are described below in the following order: the ultrasonic transceiver, the carrier board for sampling and data transfer, the sampling routine, time-of-flight calculations, the geometric tetrahedron formation of the ultrasonic transceivers and velocity calculation procedure, considerations in designing anemometers, four algorithms correcting errors caused by airflow shielding from anemometer struts and base, data filtering, and the main features of the user interface.

1) MEMS ultrasonic transceiver

The CH-101 transceivers used in the anemometer are miniature, ultra-low power ultrasonic time-of-flight range sensors, based on aluminum nitride piezoelectric micro-electromechanical system (MEMS) technology [26]. They are system-in-package integrating a micromachined piezoelectric ultrasonic transducer with SoC (system on chip) in a reflowable package (Figure 1). The SoC runs Chirp's ultrasonic digital signal processing algorithms and includes an integrated microcontroller that provides digital measurements of the ultrasonic pulse via inter-integrated circuit (I2C).

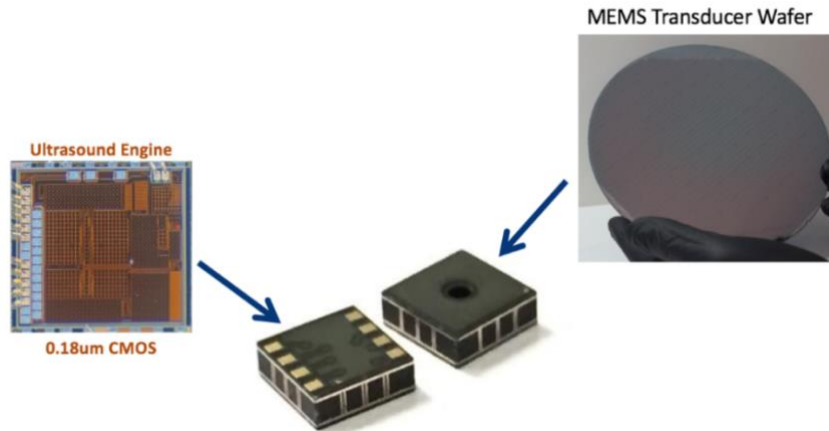


Figure 1: The CH-101 has a MEMS ultrasound transducer and a CMOS mixed-signal integrated circuit contained in a 3.5 mm square land grid array package.

The application-specific integrated circuit (ASIC) contained in CH-101 is connected to the MEMS piezoelectric membrane vibrating at a fixed frequency near 175 kHz. A similar ASIC is described in [27]. The system is designed to be triggered by a microcontroller such as the Microchip SAM-R21 on the anemometer's carrier board (described below) such that all the CH-101s in the system can be synchronized to start transmitting or recording synchronously. The CH-101 has a digital interface, a 1 m maximum range, and power consumption in the range of 10uW-1mW depending on operating mode and sampling rate.

The CH-101 runs specialized firmware to control the operation of the sensor. This firmware is optimized for each application and is loaded at run-time. The custom anemometry firmware controls the measurement process and permits the microcontroller to read out data. Each sending-receiving cycle requires about 10ms. Most of this time is to allow the ultrasound to decay to an undetectable level, so the previous pulse is not detected during the current measurement. Since each CH-101 in the system takes turn transmitting, the full time to complete one measurement is $N \cdot 10\text{ms}$, where N is the number of CH-101s. Therefore, the maximum possible measurement rate is approximately 25Hz in our anemometer containing four transceivers.

The use of pulses instead of continuous waves allows significant energy savings in the device. Figure 2 shows the approximate shape of the signal received by the ASIC. The signal's time of arrival is determined by sampling the pulse every 8 waves (dotted lines), at which points a variety of measured parameters are reported by the ASIC.

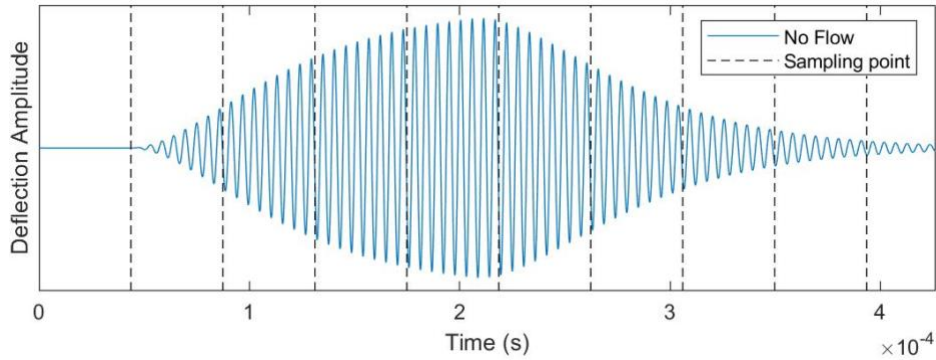


Figure 2: Receiver's membrane vibration.

The core challenge in ultrasonic anemometry is detecting an exact location on the pulse envelope that can serve as the arrival timing point, and is described in Section 3 below.

2) Carrier board; sampling routine

The carrier board is the interface between the transceivers and the outside world. Aside from the electrical requirements of the transceiver, each transceiver requires a specific initialization procedure and every measurement requires setup, precise triggering and read-out of multiple sets of data. The board also manages a wired digital thermometer used in the air velocity calculations, and includes an onboard magnetometer and accelerometer (LSM303) to convert anemometer wind direction into an absolute direction (e.g., North East). The board combines the two functionalities of sensor-carrier board and communications board, and is designed as a four-layer printed circuit board (Figure 3). The MCU communicates with the rest of the board through two I2C busses. One controls a set of port expanders (hardware that allows more than one device to connect to a single port) used for controlling the state of the four attached CH-101 transceivers, and the other is used for communicating with the transceivers, the wired thermometer, and the accelerometer/magnetometer sensor. The board is laid out in a 5 cm diameter disc (see Figure below).

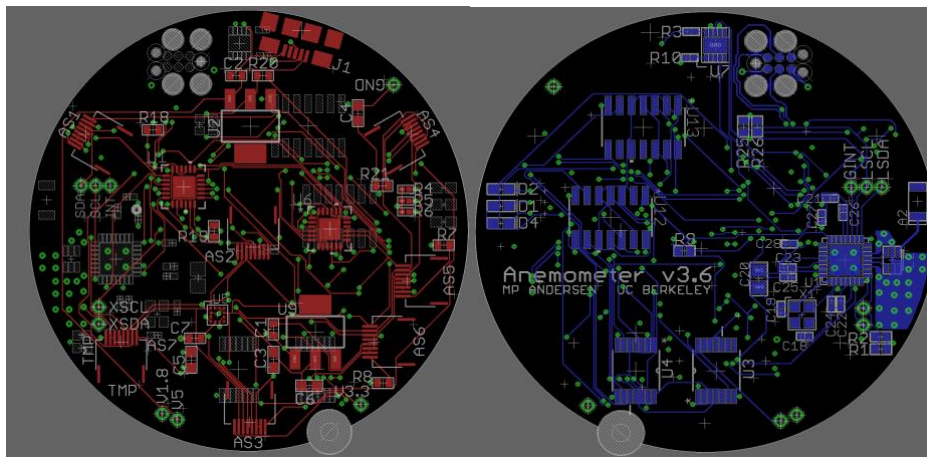


Figure 3: The four-layer carrier board. Components are mounted on both sides; the top including wiring and USB connectors is on the left (red), and the bottom with firmware flashing port and signal lights is on

the right (blue).

Data output is provided by wireless transmission (802.15.4) as well as wired output, using the system described in [28]. The anemometers can operate on internal battery or USB power. For continuously monitored wireless applications, a 19 Amp-hour D-cell battery is expected to last 0.5 years or 10 years for sampling rates respectively of one sample per second or one sample per 20 seconds. For handheld spot measurement applications, a sampling rate of six samples per second provides 80 days of continuous use.

The transmitted data describes the wave amplitude and position within the waves in the pulse (I/Q data). The anemometer's four transceivers operate in a rotating one-send-three-receive arrangement (described in section 4 below). The send-receive sequence is repeated four times within a 40ms period (Figure 4 below), yielding 12 sets of I/Q data (3 for each transmitting transceiver). Each set of I/Q data contains sixteen complex numbers. The data are bundled with the sampled thermometer, magnetometer, and accelerometer data, as well as some metadata such as the clock calibration results obtained during initialization, and transmitted over both USB and the 802.15.4 radio. Figure 5 shows the range of time scales, from the membrane vibration rate to the anemometer's user-selected airflow sampling rate (6 and 2Hz shown; the total possible range is 25 to 0.03Hz).

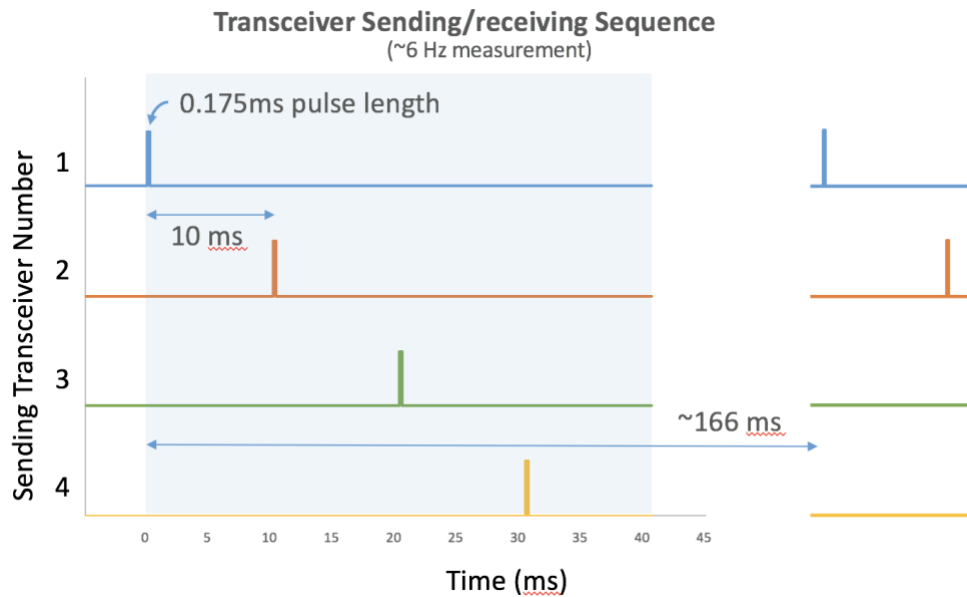


Figure 4: Sequence of transmitting among the four transceivers. Each transceiver sends a pulse in turn, separated by 10ms. The other three receive the transmission.

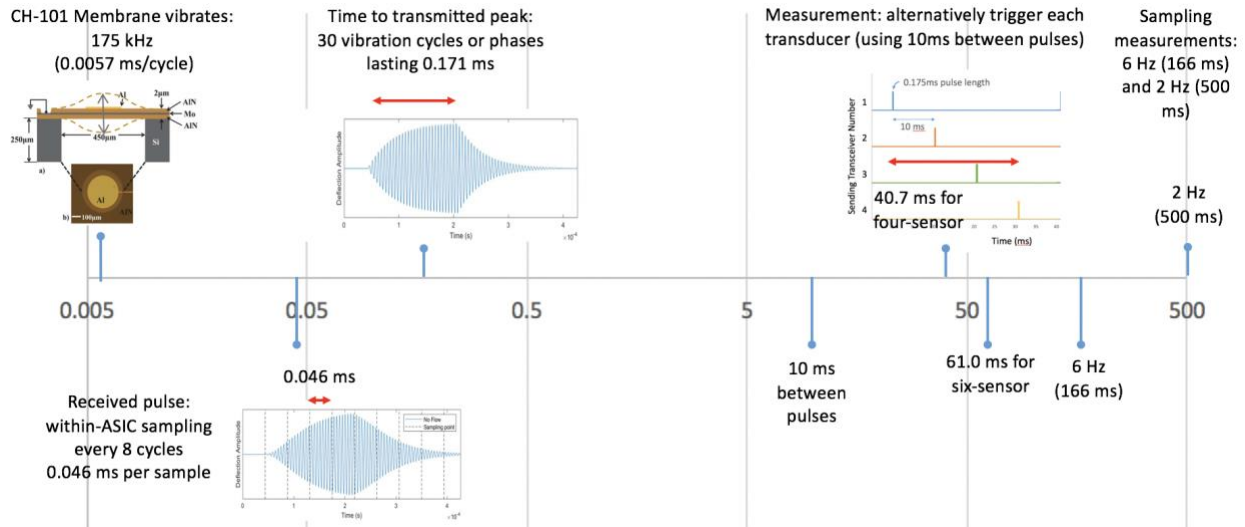


Figure 5: Logarithmic time spectrum in ms of a single anemometer measurement, from membrane vibration, to within-ASIC sampling of received pulse, to measurement of sets of 4 pulses, to the user's selected airflow sampling rate.

3) Time-of-flight calculations

The signal processing required for measuring time-of-flight (TOF) was a major development and is reported in a separate paper [29]. The following is a short summary of the method used in this anemometer.

The transceivers are arranged to create a set of sonic pathways to measure air velocity. Ultrasonic pulses travel in both directions along each path, and the difference in TOFs for the two pulses is used to calculate the air velocity along the path. Given a TOF between each transceiver pair (e.g. i and j) of our anemometer, air velocity can be calculated from the following equation:

$$\vec{v}_{i-j} = 0.5 \left(\frac{d}{TOF_{i-j}} - \frac{d}{TOF_{j-i}} \right) \quad \text{Equation 1}$$

Where v_{ij} is the air velocity from transducer i to j , d is the distance between transducers i and j , and TOF_{i-j} is the time-of-flight from transducer i to j .

The TOF of a pulse travelling in the direction of airflow decreases whereas the TOF for a pulse in the opposite direction increases.

Temperature can be also derived based on the speed of sound in air:

$$c_{i-j} = 0.5 \left(\frac{d}{TOF_{i-j}} + \frac{d}{TOF_{j-i}} \right) \cong \sqrt{\frac{\gamma k T}{m}} = 331.5 + 0.607 T \quad \text{Equation 2}$$

Where c_{i-j} is the speed of sound between transducer i and j , γ , k and m are air characteristic values (adiabatic index, Boltzmann constant, and molar mass), and T is the absolute temperature of the air.

Change in temperature has a significant impact on the sonic temperature. Since it changes the TOFs almost equally in both path directions, it can be distinguished from a change in air velocity, which increases and decreases the TOFs traveling in opposite directions.

There are two fundamental ways of timing pulse arrival, either by detecting the shape (envelope) of the pulse and using it to define a starting point that can be timed, or by identifying one of the 80 cycles within the pulse and measuring the phase angle within it to obtain a very precise measure of time. If both flight directions fall within the same cycle in the pulse, the measured difference in phase angles yields far more accurate measurements than envelope-based timing [30]. The disadvantage is that the range of air speeds that can be measured within one cycle is small, and has to be restricted further to assure that the measurements take place within the single cycle. Previous phase-based methods have typically assumed that airflow- and temperature-induced phase changes must remain within a half-wave cycle, thus limiting the measurable velocity and temperature range of such anemometers [31].

Our method overcomes this limitation by externally guiding the phase-cycle tracking process. To measure the time of flight between each transceiver pair, we employ a heuristic-based method that uses an on-board temperature sensor [29]. The measured temperature guides a search for locating the cycle of the current phase angle relative to an initial calibration phase angle. Phase is defined as $\tan^{-1}(I_i, Q_i)$, where I_i and Q_i are the in-phase and quadrature components at our discrete wave sampling points. Given a pair (i and j) of transducers' calibration phases ($\varphi_{0,i-j}$, $\varphi_{0,j-i}$) and temperature (T_0), we calculate the no-airflow phase for both TOF paths at time t ($\varphi'_{t,a-b}$, $\varphi'_{t,b-a}$) using temperature at time t (T_t). The heuristic uses the fact that the difference between the measured phases ($\varphi_{t,i-j}$, $\varphi_{t,j-i}$) and the calculated no-airflow phases are due to the air speed and not temperature. Accordingly, we adjust $\varphi'_{t,a-b}$, $\varphi'_{t,b-a}$ to make the difference in the temperature measured by the sensor and the temperature calculated by this algorithm to become zero.

4) Geometric configuration of transceivers

Existing commercially available ultrasonic 3D anemometers use six transceivers for measuring 3-dimensional flow, arranged in orthogonal or non-orthogonal paths between fixed pairs of transducers. The signals are sent and received along three sonic pathways in a single-pitch, single-catch arrangement. One exception is Yakunin's recent design [32], which uses a tetrahedral arrangement with 40kHz transducers communicating in the single-pitch, single-catch arrangement.

Such designs are not optimal because there is no redundancy should one of the sonic pathways be corrupted, such as in airstream shielding caused by the anemometer support structure. One or more of the xyz components of the air speed vector would be lost, and have to be corrected for empirically.


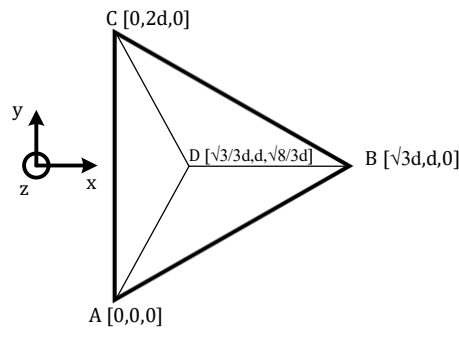
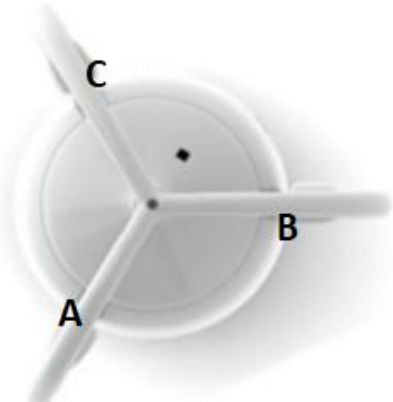
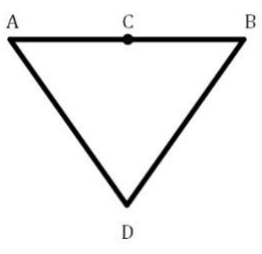
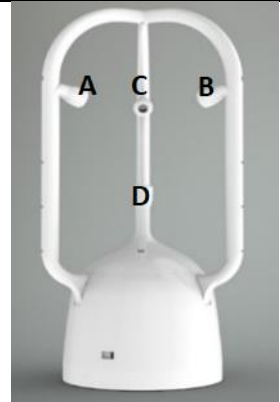
Our anemometer utilizes a tetrahedral arrangement (Figure 6a) of four transceivers. The transceivers are located at each vertex of a regular tetrahedron, operated in a single-pitch, three-catch arrangement as shown in Figures 4 and 5. This arrangement measures the 3-dimensional velocity vector with the absolute minimum possible number of transducers, but because there are *six* sonic paths between the four transceivers, there is also complete redundancy in calculating the vector should any path be corrupted. Corrupted signal paths can be ignored and the vector calculated with the remaining paths.

Since the regions of the tetrahedron that might be influenced by the wakes of the anemometer support structure are geometrically predictable, it is possible to heuristically minimize wake effects by dropping the shielded paths that occur under particular wind directions, and then if necessary applying empirical corrections to the remaining paths.

5) Calculations of velocity in the tetrahedron

All the transceivers point toward the origin (center of volume) of the tetrahedron. Relative to each other, all transceivers have the same incidence angle (angle relative to the membrane's normal). Each membrane sends and receives signals at 35 degrees incidence. Omnidirectional horns are used at the aperture of all transceivers, minimizing the effect of the angular deviation from normal.

Figure 6b shows transceivers A – D placed at each vertex. Each edge of the tetrahedron is $2d$ (~6 cm) long. The angle between any two edges is 60 degrees. The angle between the ABC plane of the tetrahedron and the edge AD is 54.74 degrees.

		
<p>Figure 6a: Tetrahedron placement of the transceivers in the anemometer</p>		
<p>Figure 6b: Geometrical configuration of top- and side views of the tetrahedron in the anemometer</p>		

The ultrasonic time of flight measurement is performed from each vertex on the isosceles tetrahedron to each of the three other vertices. There are 12 independent time of flight pairs resulting in 6 velocity measurements ($v_{AB}, v_{AC}, v_{AD}, v_{BC}, v_{BD}, v_{CD}$) using Equation 1. Cartesian components of the wind

velocity vector $\vec{v} = v_x\vec{i} + v_y\vec{j} + v_z\vec{k}$, where $\vec{i}, \vec{j}, \vec{k}$ are the unit vectors along the x, y, z axes, are calculated from the following linear equation:

$$\begin{bmatrix} v_x \\ v_y \\ v_z \end{bmatrix} = \begin{bmatrix} \frac{1}{5 \sin(30) * \cos(54.74)} & \frac{1}{5 \sin(60)} & 0 & \frac{1}{5 \cos(54.74)} & -\frac{1}{5 \sin(30) * \cos(54.74)} & -\frac{1}{5 \sin(60)} \\ \frac{1}{5 \sin(60) * \cos(54.74)} & \frac{1}{5 \sin(30)} & \frac{1}{5} & 0 & \frac{1}{5 \sin(60) * \cos(54.74)} & \frac{1}{5 \sin(30)} \\ -\frac{1}{3 \sin(54.74)} & 0 & 0 & \frac{1}{3 \sin(54.74)} & \frac{1}{3 \sin(54.74)} & 0 \end{bmatrix} * \begin{bmatrix} v_{AD} \\ v_{AB} \\ v_{AC} \\ v_{DB} \\ v_{DC} \\ v_{BC} \end{bmatrix} \quad \text{Equation 4}$$

The 3x6 matrix in Equation 4 transforms velocities on each tetrahedron edge to the overall 3D velocity. Given the 3-dimensional components of the velocity, we then calculate the overall airspeed, azimuth (angle of flow within the horizontal A, B, C plane of the anemometer), and the vertical angle (angle of flow in the plane perpendicular to the plane of the A, B, and C transceivers). Positive directions are as indicated in Figure 6 above.

$$\text{air speed} = \|\mathbf{v}\| = \sqrt{v_x^2 + v_y^2 + v_z^2} \quad \text{Equation 5}$$

$$\text{Azimuth (Horizontal Angle)} = \tan^{-1} \frac{v_x}{v_y} \quad \text{Equation 6}$$

$$\text{Vertical Angle} = \tan^{-1} \frac{v_z}{\sqrt{v_x^2 + v_y^2}} \quad \text{Equation 7}$$

6) Shaping anemometer to minimize sound reflection errors

The anemometer support structure went through several iterations to improve the ultrasonic signal quality, with the 60mm tetrahedron size fixed throughout.

Figure 7a shows the initial design of the anemometer. The support struts are 7 mm wide to house the 4 mm ribbon cable connecting the CH-101 transceivers to the carrier board, and the small green square elements are the transceivers mounted flush with the struts. In this arrangement, the adjacent anemometer struts were found to reflect ultrasonic waves into the receivers before the end of the signal pulse, creating an additive wave in the receiving membrane's impulse vibration. In order to remove this reflected noise from TOF measurement, there needed to be increased distance between receiver and struts.

The total distance between the transmitter, the closest reflective surface to both transmitter and receiver, and the receiver, should be greater than the direct distance between transmitter and receiver plus the distance traveled by the ultrasonic waves between the onset and the peak of the arriving pulse (reflections arriving after the peak do not influence TOF measurement). In order to completely avoid any detrimental reflections in our anemometer, the distance from a transceiver to the closest reflecting strut surface should be greater than 2 cm. We added 'spurs' to hold transceivers inboard of their previous location on the struts, and upward from the lid on the base of the anemometer.

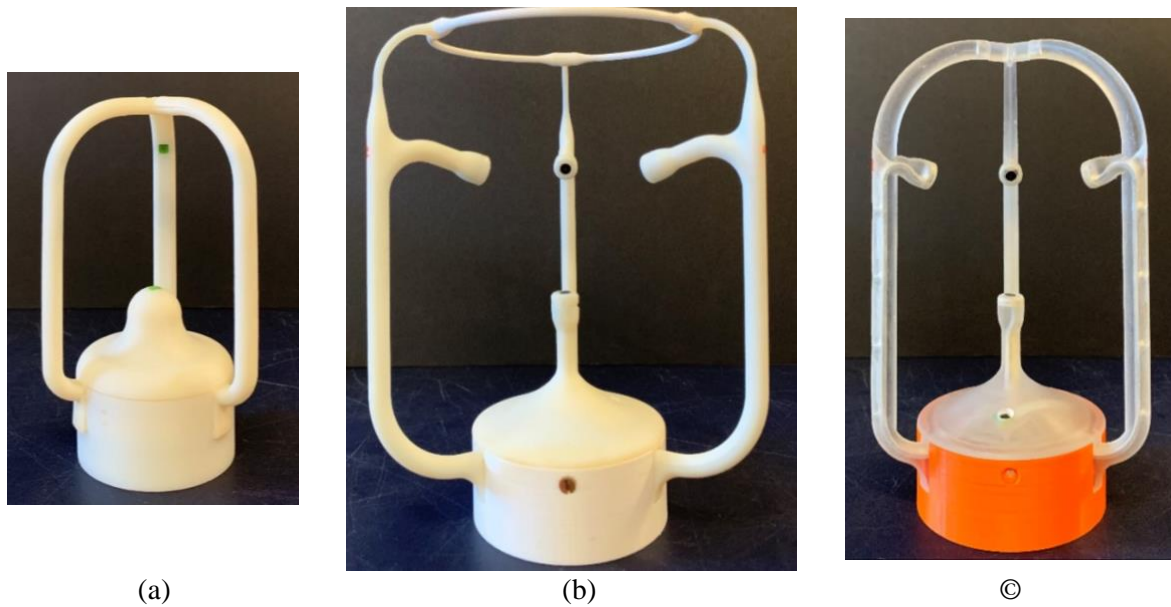


Figure 7: (a) Original design without spurs, (b) Max design, (c) Min design

The ‘Max’ anemometer in Figure 7b with 2.5 cm spurs exceeded this acoustic requirement and had the lowest TOF noise on each path of all tested designs. However the expanded bulk of the instrument could be inconvenient for some applications, so we examined the practical acoustical and aerodynamic effects of moving the struts closer inboard (Figure 7c). The ‘Min’ design with shorter spurs (1 cm) was found to have manageable reflected noise. In this design, we minimized the reflective surface area by giving the struts an outward-facing-teardrop cross-section.

Some Max and Min bodies have added space in the base for a D-cell-sized Li-ion battery (the Min version of this is seen in Figure 6). These designs have the same acoustic properties as in Figure 7b and 7c.

7) *Minimizing the aerodynamic shielding by anemometer support struts and base on the measurements within the tetrahedron.*

In the literature on outdoor ultrasonic anemometry [21–24], the problematic shielding is caused by the upwind transducer, when all or part of its wake extends down the sonic path between a pair of transducers. The corrections for flow distortion and shielding are functions of the angle between the wind direction and the acoustic path; the (width of the transducer head) / (length of sonic path) is the most important variable. Limits and correction factors are applied using an approximation of this wind angle, which introduces a potential source of error. Shielding from the support struts of outdoor anemometers is typically less than from their transducer heads (because these anemometers are large, having fewer size constraints than indoor instruments). In the literature, shielding corrections have not been found to vary with wind speed.

The tetrahedral sensor arrangement with multi-catch signaling is different from the paired-sensor arrangements of existing 3D anemometers. Because the tetrahedron’s support structure is a generic geometry, with shielding effects unlike those of existing ultrasonic anemometers, a detailed description of our shielding correction algorithms may have general utility.

Our anemometer does not approximate angles for imposing correction factors, but uses TOF measurements along the redundant paths to trigger the application of different types of corrections. Because the anemometer has three support struts and a base enclosure that are relatively near the measurement zone, their shielding can be significant. But because the different possible wind approach directions produce generic types of shielding along the sonic paths, we are able to formulate algorithms that either drop or modify the shielded paths in the transformation matrix (Equation 4). In some types, the redundancies in the six tetrahedron pathways allow shielded paths to be excluded from the calculation and replaced with measurements from paths that are unaffected. In others, empirically derived corrections are applied. We define four types of shielding below and explain the heuristics for each.

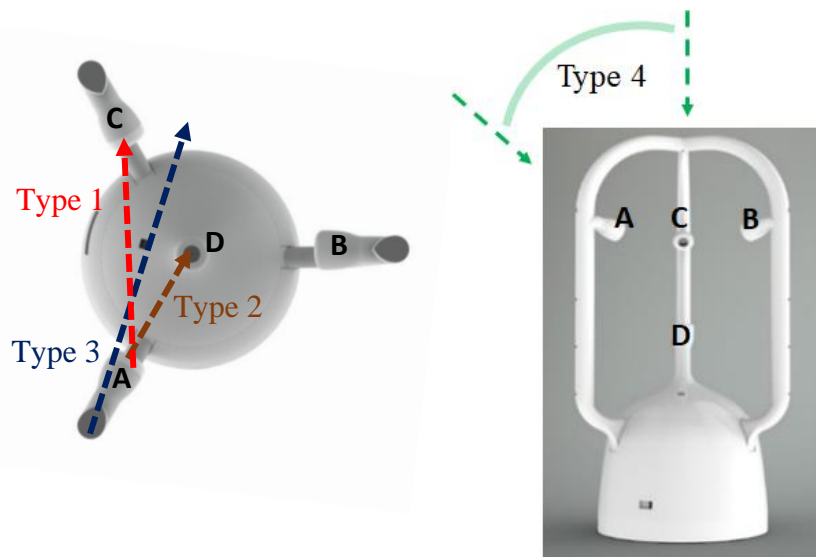


Figure 8. Geometrical configuration of different types of shielding in the tetrahedron (top and side view)

Type 1 heuristic for support-strut shielding in the horizontal (ABC) plane:

A flow that is parallel to any path (AB, AC, or BC paths; see Figure 6) in the top triangle would be partially shielded by the upwind spur and strut. As seen in Figure 8, path AC is shielded by the strut holding transceiver A, so using TOF measurements from that path will cause errors in the velocity calculations. We empirically defined situations within which we drop all measurements from the top triangle paths (AB, AC, and BC paths) and only use the bottom triangle paths (AD, BD, and CD paths) in the calculations. In this heuristic, if TOF difference in any path involving transceiver D is almost zero while the other two paths involving D are almost equal and non-zero, we then infer we are experiencing Type 1 shielding. In the illustration, BD would be the path indicating zero velocity since the airflow is perpendicular to it.

In Algorithm 1, we empirically define a correction range based on the velocities measured along AD-BD-CD paths. In this range, we modify the Equation 4 transformation matrix to retain only elements that are not impacted by the shielding. It should be noted that we cannot drop only the single impaired path in the ABC top triangle and continue to use the remaining paths of the triangle, because all three paths are required for calculation in the matrix.

Algorithm 1:

if $\left(0 < \frac{|v_{CD}|}{|v_{AD}|} < 0.5 \ \& \ 0 < \frac{|v_{CD}|}{|v_{BD}|} < 0.5\right)$ or $\left(0 < \frac{|v_{AD}|}{|v_{BD}|} < 0.5 \ \& \ 0 < \frac{|v_{AD}|}{|v_{CD}|} < 0.5\right)$ or $\left(0 < \frac{|v_{BD}|}{|v_{AD}|} < 0.5 \ \& \ 0 < \frac{|v_{BD}|}{|v_{CD}|} < 0.5\right)$:

$$\begin{bmatrix} v_x \\ v_y \\ v_z \end{bmatrix} = \begin{bmatrix} \frac{1}{3 \sin(30) * \cos(54.74)} & 0 & 0 & \frac{1}{3 \cos(54.74)} & -\frac{1}{3 \sin(30) * \cos(54.74)} & 0 \\ \frac{1}{2 \sin(60) * \cos(54.74)} & 0 & 0 & 0 & \frac{1}{2 \sin(60) * \cos(54.74)} & 0 \\ -\frac{1}{3 \sin(54.74)} & 0 & 0 & \frac{1}{3 \sin(54.74)} & \frac{1}{3 \sin(54.74)} & 0 \end{bmatrix} * \begin{bmatrix} v_{AD} \\ v_{AB} \\ v_{AC} \\ v_{DB} \\ v_{DC} \\ v_{BC} \end{bmatrix}$$

Type 2 heuristic for support strut shielding of vertical (z-axis) plane:

Any airflow whose azimuth aligns with that of a path involving the bottom transducer D is blocked by the strut of that path. As seen in Figure 8, path AD is shielded along its length by the strut holding transceiver A. Using AD measurements would cause significant error (considerably larger than Type 1 errors). We developed an empirically defined azimuth angle range in which measurements from the bottom triangle paths (AD, BD, and CD paths) are dropped for the v_x and v_y calculation, but are used for the v_z calculation. In this heuristic, if the velocity of any path in the top triangle is almost zero while other two paths in the top triangle are almost equal and non-zero and meet some direction criteria (see Algorithm 2 for details), then we can infer that we are experiencing Type 2 shielding by an upwind strut. In the case of AD wind direction, velocity along the perpendicular path BC will be near zero.

In algorithm 2, we empirically define a correction range based on the airspeed measured in the AB-AC-BC paths. In this range, we modify the matrix from Equation 4 using only the elements not impacted by the shielding of any one of the AD-BD-CD paths. As with heuristic Type 1, we cannot drop a single path (e.g., path AD) and keep the other two (BD and CD), since values for all three paths are needed for 3D calculation.

Algorithm 2:

if $\left(0 < \frac{|v_{BC}|}{v_{AB}} < 0.5 \ \& \ 0 < \frac{|v_{BC}|}{v_{AC}} < 0.5\right)$ or $\left(-0.5 < \frac{|v_{AB}|}{v_{AC}} < 0 \ \& \ -0.5 < \frac{|v_{AB}|}{v_{BC}} < 0\right)$ or $\left(-0.5 < \frac{|v_{AC}|}{v_{AB}} < 0 \ \& \ 0 < \frac{|v_{AC}|}{v_{BC}} < 0.5\right)$:

$$\begin{bmatrix} v_x \\ v_y \\ v_z \end{bmatrix} = \begin{bmatrix} 0 & \frac{1}{2 \sin(60)} & 0 & 0 & 0 & -\frac{1}{2 \sin(60)} \\ 0 & \frac{1}{3 \sin(30)} & \frac{1}{3} & 0 & 0 & \frac{1}{3 \sin(30)} \\ -\frac{\alpha}{2 \sin(54.74)} & 0 & 0 & \frac{\alpha}{2 \sin(54.74)} & \frac{\alpha}{2 \sin(54.74)} & 0 \end{bmatrix} * \begin{bmatrix} v_{AD} \\ v_{AB} \\ v_{AC} \\ v_{DB} \\ v_{DC} \\ v_{BC} \end{bmatrix}$$

Note that the modified Equation 4 matrix now only includes paths of the ABC plane (top triangle) to be used for v_x and v_y calculations, while using α to correct the AD-BD-CD paths for the vertical component (since we do not have redundancy here to allow their removal). The factor α is 1 when the airflow in plan view is not parallel to that path (e.g., BD and CD) and becomes an empirically selected value when it is parallel to the path (e.g., AD).

Type 3 heuristic for support-strut shielding of adjacent horizontal and vertical paths:

In situations where Types 1 and 2 shielding are simultaneously impacting the sonic paths' velocity measurements, the Type 3 heuristic compensates for these combined impacts. It happens when a path from the horizontal plane (e.g., AC in Figure 8) and a path from the paths involving bottom transceiver (e.g., AD) are partially shielded by the common transceiver strut (e.g., strut adjacent to A). Both AC and AD paths could experience some shielding along their edges. We found that under these conditions, the direct use of measurements from these paths causes significant errors. An empirically defined correction range is used, in which measurements from both paths (e.g., AC and AD) are modified based on the measurements from other paths. As with the other heuristics, the correction range in which this heuristic is triggered is empirically defined.

In Algorithm 3, we empirically define a range of angles based on the airspeed vector measured by paths in the top and bottom triangles. Within this range, we modify two elements in the matrix from Equation 4. As with heuristic Type 2, we cannot drop any paths since we do not have redundant un-impacted values.

Algorithm 3:

$$\left(\text{if } \left(0.2 < \frac{|v_{CD}|}{|v_{AD}|} < 0.8 \ \& \ 0 < \frac{|v_{CD}|}{|v_{BD}|} < 0.5 \right) \text{ or } \left(0.2 < \frac{|v_{AD}|}{|v_{BD}|} < 0.8 \ \& \ 0 < \frac{|v_{AD}|}{|v_{CD}|} < 0.5 \right) \text{ or } \left(0.2 < \frac{|v_{BD}|}{|v_{AD}|} < 0.8 \ \& \ 0.2 < \frac{|v_{BD}|}{|v_{CD}|} < 0.8 \right) \right) \ \& \ \left(\text{if } \left(0.2 < \frac{|v_{BC}|}{v_{AB}} < 0.8 \ \& \ 0.2 < \frac{|v_{BC}|}{v_{AC}} < 0.8 \right) \text{ or } \left(-0.8 < \frac{|v_{AB}|}{v_{AC}} < 0.2 \ \& \ -0.8 < \frac{|v_{AB}|}{v_{BC}} < 0.2 \right) \text{ or } \left(-0.8 < \frac{|v_{AC}|}{v_{AB}} < 0.2 \ \& \ 0.2 < \frac{|v_{AC}|}{v_{BC}} < 0.8 \right) \right) :$$

$$\begin{bmatrix} v_x \\ v_y \\ v_z \end{bmatrix} = \begin{bmatrix} \frac{\gamma}{5 \sin(30) * \cos(54.74)} & \frac{\gamma}{5 \sin(60)} & 0 & \frac{\gamma}{5 \cos(54.74)} & -\frac{\gamma}{5 \sin(30) * \cos(54.74)} & -\frac{\gamma}{5 \sin(60)} \\ \frac{\beta}{5 \sin(60) * \cos(54.74)} & \frac{\beta}{5 \sin(30)} & \frac{\beta}{5} & 0 & \frac{\beta}{5 \sin(60) * \cos(54.74)} & \frac{\beta}{5 \sin(30)} \\ -\frac{\alpha}{3 \sin(54.74)} & 0 & 0 & \frac{\alpha}{3 \sin(54.74)} & \frac{\alpha}{3 \sin(54.74)} & 0 \end{bmatrix} * \begin{bmatrix} v_{AD} \\ v_{AB} \\ v_{AC} \\ v_{DB} \\ v_{DC} \\ v_{BC} \end{bmatrix}$$

The matrix includes compensation factors (α , β , and γ) for paths impacted by the shielding. These factors are always 1 except for cases where their associated values in the velocity vector have been impaired. For these cases, we empirically determined the factors through trial and error. They have different yet constant values within their correction ranges. To improve performance, they might eventually be made into variables based on the relationships between path velocities.

Type 4 heuristic for flow reduction by anemometer base:

At high angles of descending wind (pitch angle between -45° and -90°) the airflow vertical component (v_z) is reduced by shielding from overhead struts, and from the flow deflection through the tetrahedron caused by the anemometer base downstream of the tetrahedron. The reduction is along the paths relating to v_z (AD, BD, or CD) (Figure 8). Although the overhead struts above the tetrahedron level are narrow and streamlined, and the base is distanced from the tetrahedron and aerodynamically streamlined, there is an observable airflow reduction in the v_z . The effect depends also on whether the anemometer is resting on a surface or suspended in space. We empirically defined a correction range above the -45° threshold in which the calculated vertical velocity increases linearly with the calculated vertical approach angle. The coefficients shown below obtain to the anemometer shown in Figure 4B; they would be less for the more streamlined design in Figure 4C, and more for instances when the anemometer is resting on a table. The table surface acts to turn the downward airflow direction into a lateral direction within the volume of the tetrahedron.

Algorithm 4 uses the vertical angle calculated from the velocities measured in the bottom triangle paths. Above the threshold, it multiplies v_z by the factor shown below.

Algorithm 4:

if Vertical Angle $< -45^\circ$:

$$v_z = v_z * \left(1 - 0.9 * \frac{(\text{Vertical Angle} + 45)}{100} \right)$$

8) User interface

A description of the interface gives a sense of the device capabilities. There are three screens, one main and two diagnostic. The main screen presents the integrated results (Figure 9). Two diagnostic screens (not shown) present for the six individual sonic paths: 1) path velocities and temperatures, 2) bidirectional phase angles. The user has control over the median filter length, sampling rate choice, and data save options.

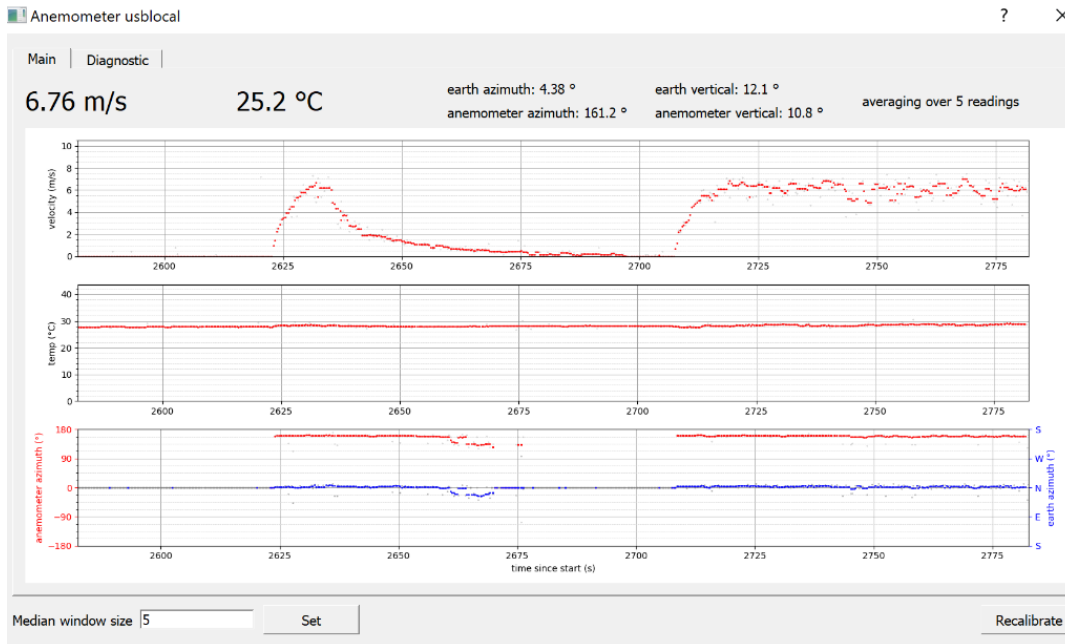


Figure 9: Interface main screen time-series charts of air speed, temperature, and wind azimuth relative to anemometer (red) and to magnetic north (blue). Wind vertical approach angle and turbulence intensity are numerical values. Azimuth values are not displayed for air speeds below 0.05m/s.

The median filter is used to remove occasional random spikes from the measurements. The window length of the filter is selected in the user interface to adjust the response speed to the application at hand. For applications where you want the responsiveness of handheld anemometers, using a 2 Hz or 6 Hz measurement frequency together with a window length around 5 provides rapid signal responsiveness while filtering out typical spikes.

Validation testing and results

We tested the anemometer in the upper gradient-wind level of our open-circuit boundary layer wind tunnel (measurements at 1.2m height in the 1.52m high, 2.13m wide cross section). At this height the tunnel has low natural turbulence intensity (under 3%) of mean air speeds at 2m/s.

Although it is possible to suppress the tunnel turbulence intensity to levels around 1%, it has been suggested [23,33,34] that testing in such laminar flow may increase the size and stability of vortices behind anemometer struts over those that occur in natural air flows, leading to overcorrections in the heuristics. Conversely, it would be useful to test at higher turbulence levels, such as 10 or 20%, both because these are more typical of indoor air flows, and the turbulent fluctuations might provide a stress test of the direction-sensitive shielding correction algorithms. We are currently planning a future investigation of anemometer performance under higher turbulence, but initially the low turbulence tests provide a cleaner view of the shielding corrections. .

All data were collected in 60-second periods. We referenced ultrasonic air speeds against adjacent measurements from two hotwire sensors calibrated in a NIST-certified calibration wind tunnel using a differential pressure sensor (Omega model WT4401-S, [35]). The hotwire sensor models were SensoData 5500 [15] and TSI 9515 [14]. In addition, an outdoor ultrasonic anemometer (Young model 81000) [36] was measured alongside for comparing mean and turbulence measurements. Wind approach angles were

obtained using a protractor-equipped Bogen tripod support. We obtained azimuthal (yaw) angles by horizontally rotating the anemometer, and downward- and upward-directed airflow angles (respectively negative and positive pitch) by tilting it forward and backward relative to the flow.

Unshielded airspeed measurements: With the anemometer in a no-shielding condition (0° yaw angle), we collected data for 10 different air speeds (0, 0.5, 1, 1.5, 2, 2.5, 3, 3.5, 4, 4.5, 5 m/s). Six m/s is the upper limit for the hotwire sensors. Figure 10 shows the air speed comparison. For our anemometer, the mean absolute error is 0.11 m/s and the normalized mean absolute error is $\pm 4.0\%$ of reading ($\pm 1\%$ of full scale). For the RM Young anemometer, the mean absolute error is 0.20 m/s and the normalized mean absolute error is $\pm 7.7\%$ of reading. These values are within the accuracies reported for commercial hotwire and meteorological ultrasonic anemometers.

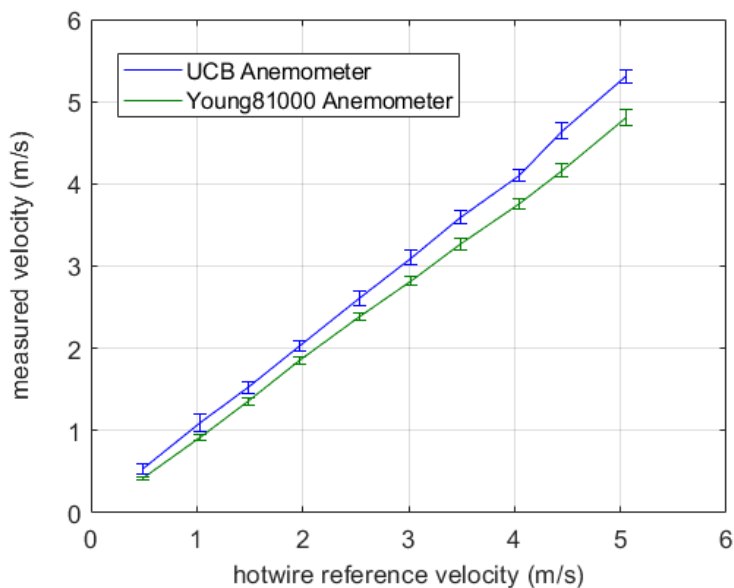


Figure 10. Ultrasonic air speed vs hot wire measurements, unshielded condition

Turbulence intensity: We compared TI measurements from the two ultrasonic anemometers over a range of wind tunnel velocities, using a 60sec measurement interval at each velocity. Both anemometers were adjacent and measuring the same time interval. Their outputs can only be compared qualitatively, because their internal processing is not the same. Our ultrasonic anemometer is sampling at 6 Hz, resulting in 360 samples over the 60 seconds. A variable-length median filter is available for suppressing spike values. The TI is the standard deviation (SD) of the filtered samples divided by their mean. Figure 11 presents TI values with two widely differing median filters applied (3- and 15-measurement lengths). With no filter, the highest value at 0.5m/s is 0.2. In contrast, the Young 81000 collects measurements at 25 Hz but internally processes 20 readings before outputting single values for mean and SD, resulting in a 1.25 Hz sample rate and 75 samples over the 60 sec. We evaluated TI for the Young 8100 in two ways: 1) we calculated the TI value for each sample by dividing the SD by its associated mean, and then averaged the 75 TI values. 2) We calculated the standard deviation of the 75 mean values, and divided by their overall mean. The two methods describe high- and low-frequency components of turbulence measured by the Young 8100. Our ultrasonic TI is close to that of the Young 8100 at higher wind tunnel velocities but reads higher values at lower velocities, especially at 0.5 to 1m/s. At this stage we cannot define the

causes of the differences in output of the two anemometers; a comprehensive evaluation of turbulence is planned.

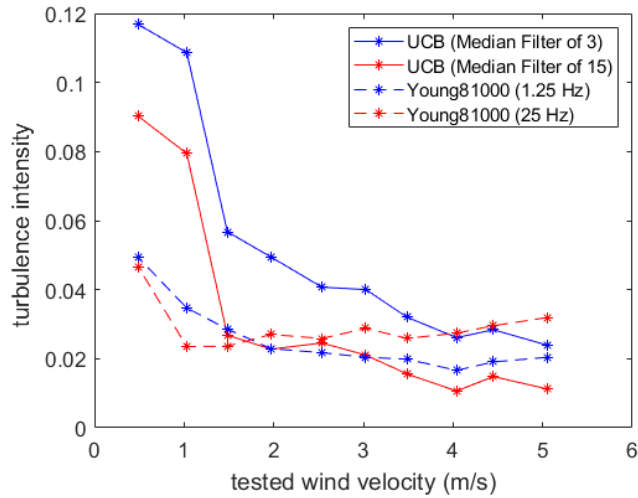


Figure 11. Turbulence intensity measured in the anemometer’s unshielded yaw orientation

Three-dimensional angle and speed measurements: We tested the anemometer’s measurements across the full functional ranges of both yaw (azimuth) and pitch (vertical wind angle), by rotating the anemometer to each of the fixed angles shown in Table 1. The tests measure the effectiveness of the fundamental equations and the shielding algorithms. The wind tunnel air speed was 5 m/s.

Table 1. Yaw and pitch axes: tested angles

Rotation axis	Angles
Yaw axis	-170, -160, -150, -140, -130, -120, -110, -100, -90, -80, -70, -60, -50, -40, -30, -20, -10, 0, 10, 20, 30, 40, 50, 60, 70, 80, 90, 100, 110, 120, 130, 140, 150, 160, 170, 180
Pitch axis	-90, -75, -65, -55, -45, -35, -25, -15, 0, 15, 25, 35, 45, 55, 65

Yaw angles and speeds: Figure 12 shows the actual and measured yaw angles from a horizontal rotation test. The average error is 3.1° with SD 2.62° . At certain angles the error is higher (e.g. $\pm 20^\circ$, $\pm 80^\circ$, 130°), contributing much of the measured SD. As these error angles are related to the geometry of the struts surrounding the tetrahedron, they may be empirically correctable. However at this stage we consider the unadjusted angle determination to be very good.

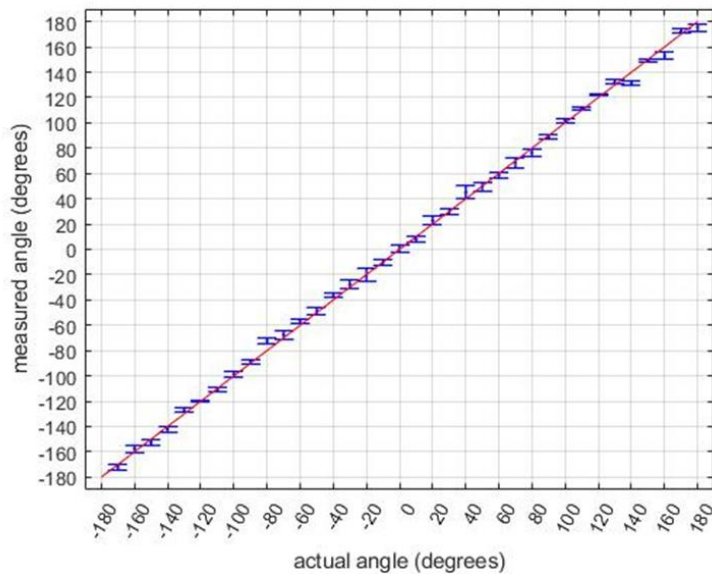


Figure 12. Actual yaw (azimuthal) angles vs measured angles in the horizontal rotation test

Figure 13 shows measured airspeeds through 360 degrees of horizontal rotation, at two wind tunnel speeds (3.5 and 1.0 m/s). The mean absolute error is 0.11 m/s with SD 0.07 m/s, and the mean normalized error is 2.26 % with SD 1.41%. There is little meaningful biased error in the airspeed measurements. One exception might be the recurrence of low readings from the Min design at the border between Types 1 and 3 heuristics; the exact position of this border might warrant examination.

A rotation test at 0.18 m/s absolute (not plotted), yielded an overall measured mean of 0.17 m/s, overall mean absolute error of 0.025 m/s, and SD of the mean absolute errors measured for all angles of 0.017 m/s. At 0.31 m/s absolute, the overall mean was 0.27 m/s, overall mean absolute error 0.05 m/s, and the SD of the mean absolute errors for all angles was 0.028 m/s.

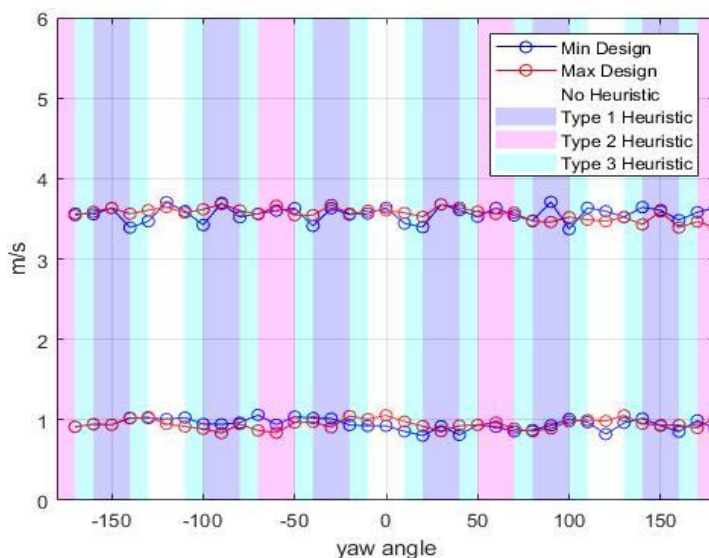


Figure 13. Measured air speeds from rotating two anemometer designs, at two wind tunnel air speeds.

Pitch angles and speeds: We performed pitch axis tests for all upward- and downward-directed flows, repeating them at the three yaw angles (0°, 30°, and 60°) that represent the greatest range of shielding effects from the struts. There is no shielding at 0° yaw until the flow approaches vertical and the overhead struts have an effect (triggering the Type 4 heuristic). At 30° and 60° yaw, the struts shield the airflow along one or more paths and heuristics are triggered. At 30° yaw, the shielding error is induced along one of the top triangle paths (A to B in Fig 9), while at 60° yaw, the error comes from the shielding by the upstream anemometer arm of the upstream vertical path (A to D in Fig 10).

Figure 14 shows the anemometer's usable range of pitch angles for the three yaw cases. Upward flows greater than 35° above horizontal are being distorted by the presence of the anemometer base, causing the pitch to be underestimated for all yaw angles. All other angle predictions are close to the actual, including those for vertical downward air flows. The mean error across all pitch angles for 0° yaw is 3.03°, with 3.93° SD; at 30° yaw the mean error is 2.77° with 4.14° SD, and at 60° yaw mean error is 3.90° with 3.74° SD.

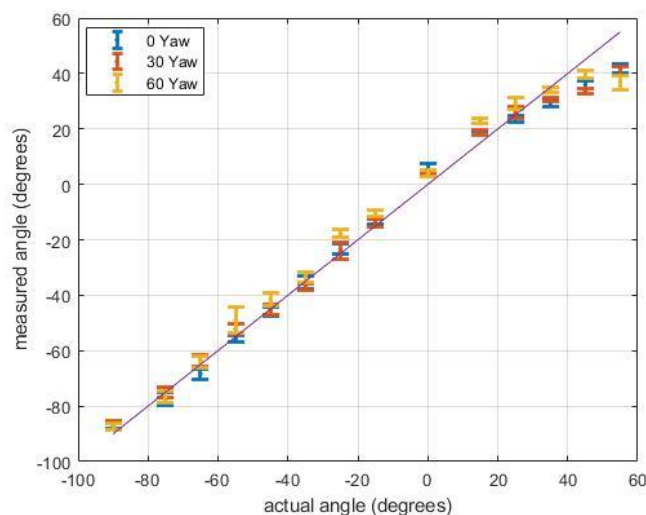


Figure 14. Measured vs actual pitch axis angles, for 3 different angles of yaw

Figure 15 shows the measured air speeds for the full range of pitch angles. The wind tunnel air speed was 3.3 m/s. As expected, the error is high at the highest upward pitch (+55 degrees) where the flow is shielded by the anemometer base. At the +45 degrees pitch, the air speed measurement is close to the actual air speed, although the previous figure has shown that the measured pitch angle is being affected by the base at that pitch. The mean absolute error is 0.07 m/s (0.06 m/s in 0° yaw, 0.08 m/s in 30° yaw, and 0.06 m/s in 60° yaw) or normalized error of 2.17 % (1.90 % in 0° yaw, 2.72 % in 30° yaw, and 1.88 % in 60° yaw) for pitch angles between -90 and 45 degrees. The mean absolute error is 0.11 m/s and normalized error is 3.46 % for pitch angles between -90 and 45 degrees.

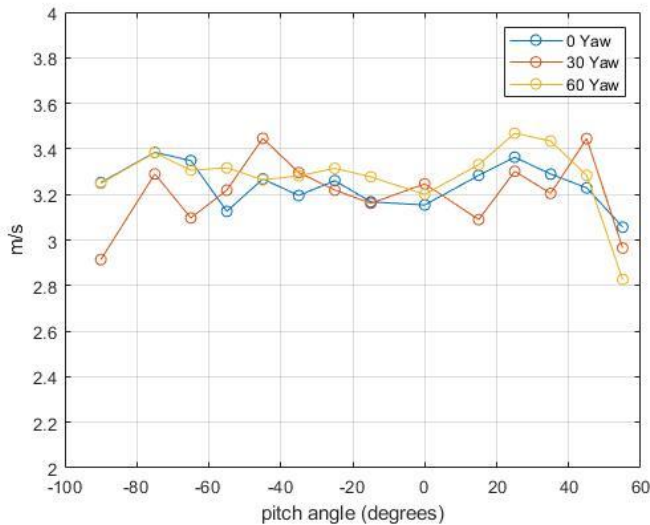


Figure 15. Air speed variation by pitch angle, at 0°, 30, and 60° in yaw axis

Discussion

Currently:

- 1) Our prototype anemometers' components such as the fabricated carrier board, cables, and temperature sensor total less than \$100 retail in small quantities. At large scale we would expect the prices to be lower. Since the digital transceivers (four CH-101's) are manufactured on wafers, they are inherently less expensive than ultrasonic transceivers currently on the market. We have been 3D printing enclosures ourselves; these would be injection molded in a commercial product, and become inexpensive in large-scale production. Assembly is entirely snap-together of fabricated parts with cable connectors pre-mounted on transceivers and carrier board. There is no calibration needed except for setting the magnetic compass parameters. Commercially produced versions may therefore be inexpensive to assemble compared to anemometers currently on the market.
- 2) The anemometer's three-dimensional measurement accuracy across a wide range of wind angles and wind speeds is unprecedented for inexpensive indoor instruments. Advances in the commercialized production of the CH-101 transceiver, and in the control software reported above, will presumably improve this performance.
- 3) The ability to acquire data over time, either over our open-source 802.15.4 radio platform, or over USB wire, is also unprecedented for a low-cost instrument.
- 4) The power requirements of the system in wireless mode are currently sufficiently low that they enable battery-life numbers in years, which makes the anemometer useful for long-term untethered building monitoring applications. Sampling frequencies of 2 Hz and below are appropriate for most types of long-term indoor monitoring applications, while extending the battery life linearly. The 6 Hz used in this paper provides high responsiveness for real-time diagnostic use.
- 5) We have discussed in this paper mostly the Min anemometer. The more widely spaced Max has inherently better aerodynamic performance (e.g., see Figure 13). But for indoor applications, Min

results as corrected by our heuristics are not greatly different from those of Max and give us a conservative estimate of the anemometer's future performance. In addition, we have two versions of the upper part of both the Min and Max anemometers—curved struts converging into a 3-way star, versus a ring-top. The star version (Min example shown in Figure 7c) facilitates suspension from a string. Although the overhead struts do shield the sonic paths under vertical downward flows, we have minimized shielding by making the struts narrow and streamlined above the level of the transceiver spurs. The correction in heuristic Type 4 then compensates for the remainder. The ring-topped versions of either anemometer (Max example shown in Figure 7b) eliminate the star's direct overhead shielding and so might be preferred for making measurements where downward flows predominate, as in clean rooms, surgical suites, or under ceiling fans.

- 6) The current anemometer has been shown to be able to measure speed below 0.2 m/s for all azimuthal directions with fair accuracy (0.02 m/s MAE). The current 6cm sonic pathlength, sampling at 6 Hz, is capable of oversampling turbulence at the frequencies affecting human comfort perception (~1Hz). At this point, we have not systematically referenced the anemometer's turbulence measurements against those of high-frequency hotwires or laser Doppler instrumentation.

In the future:

- 7) Higher sampling rates, up to 25Hz, will be examined for measuring airflow turbulence, against detailed velocity and temperature reference conditions.
- 8) We anticipate an improved automatic recalibration procedure that takes advantage of our redundant sonic paths to continuously search for periods of time when air movement around the anemometer has stopped. During these times our calibration constants can be updated.
- 9) Even though the tetrahedron-based 3-dimensional velocity equations are completely closed-form, and the four shielding compensation algorithms are also based on the anemometer geometry, the wind directions within which the shielding algorithms are triggered were determined empirically. We optimized these angles and algorithms until the air velocity and direction errors reached an acceptable level of accuracy. They would naturally be tuned further in commercial product development. In their present form, they give us a conservative estimate of the ultimate accuracy possible in such a compact anemometer design.
- 10) As the CH-101 moves into production, its acoustic power level has increased. We understand that this will allow a dust/moisture filter to be installed at the inlet to the transceivers without causing a loss in performance.
- 11) The current design is limited at detecting *upward* airflows at angles greater than 45° due to shielding from the anemometer base. The anemometer must be oriented on its side or inverted to capture upward flows. In a future less compact design the carrier board/battery enclosure could be distanced from the tetrahedron and connected to it via stalk or cable, providing unobstructed omnidirectional measurements.
- 12) In a future commercial version, it may be possible to employ different cabling than our 4mm wide ribbon cable. This would allow the current 7mm strut diameter and its shielding level to be reduced.

Conclusion

In the past, it has been practically and economically difficult to monitor 3-dimensional indoor air velocity in buildings. Having sensitive feedback about airspeed and direction should enable new applications that manage building air movement. Air streams of appropriate direction and speeds underlie the comfort and safety of occupants, the effectiveness of ventilative cooling and pollutant removal, and the building systems' energy use. By adopting new high-frequency silicon-based MEMS transceivers used in ultrasonic range-finding, we have developed an inexpensive three-axis anemometer of unusual sensitivity for indoor environment applications. The anemometer is compact, measures temperature, and contains features like an onboard compass/tilt sensor to continually correct the anemometer's coordinates to those of the Earth. The anemometer measures TOF between its transceivers from the phase angle of one wave cycle within the transmitted ultrasonic pulse; a novel algorithm uses the on-board temperature measurements to track the cycle being measured. Unlike other ultrasonic anemometers that require three dedicated pairs of transceivers, this design employs a tetrahedron configuration of four ultrasonic transceivers cycling in a one-send three-receive mode. This is the minimum number of transducers capable of capturing a 3-dimensional flow, while also providing complete redundancy in the data needed to calculate the vector. Unique algorithms use the redundancy to infer and eliminate errors from the aerodynamic wakes shed by the anemometer's struts and base. This paper describes both the hardware and software of the anemometer. Validation testing shows that the anemometer prototypes have high accuracies in measuring velocity, temperature, and the azimuthal and vertical angles of wind direction.

Acknowledgements:

This work was supported by the California Energy Commission Electric Program Investment Charge (EPIC) Contract Number: EPC-14-013, "Low-Cost MEMS-Based Ultrasonic Anemometer for Use Indoors and in HVAC Ducts". We also thank Andy Wang for writing code for the data analysis.

References

- [1] ANSI/ASHRAE, Standard 55 – Thermal Environmental Conditions for Human Occupancy, Atlanta, 2017. doi:ISSN 1041-2336.
- [2] G. Paliaga, H. Zhang, T. Hoyt, E. Arens, Eliminating overcooling discomfort while saving energy, ASHRAE J. April (2019) 14–28.
- [3] J. Toftum, Air movement - good or bad?, Indoor Air. 14 (2004) 40–45. doi:10.1111/j.1600-0668.2004.00271.x.
- [4] H. Zhang, E. Arens, S.A. Fard, C. Huizenga, G. Paliaga, G. Brager, L. Zagreus, Air movement preferences observed in office buildings, Int. J. Biometeorol. 51 (2007) 349–360. doi:10.1007/s00484-006-0079-y.
- [5] S. Schiavon, A.K. Melikov, Energy saving and improved comfort by increased air movement, Energy Build. 40 (2008) 1954–1960.
- [6] A.K. Melikov, Advanced air distribution: Improving health and comfort while reducing energy use, Indoor Air. 26 (2016) 112–124. doi:10.1111/ina.12206.
- [7] S. Liu, A. Lipczynska, S. Schiavon, E. Arens, Detailed experimental investigation of air speed field induced by ceiling fans, Build. Environ. 142 (2018) 342–360. doi:10.1016/j.buildenv.2018.06.037.
- [8] Y. Gao, H. Zhang, E. Arens, E. Present, B. Ning, Y. Zhai, J. Pantelic, M. Luo, L. Zhao, P. Raftery, S. Liu, Ceiling fan air speeds around desks and office partitions, Build. Environ. 124 (2017). doi:10.1016/j.buildenv.2017.08.029.
- [9] T. Parkinson, A. Parkinson, R. de Dear, Continuous IEQ monitoring system: Performance

- specifications and thermal comfort classification, *Build. Environ.* 149 (2019) 241–252. doi:10.1016/j.buildenv.2018.12.016.
- [10] T. Parkinson, A. Parkinson, R. de Dear, Continuous IEQ monitoring system: Context and development, *Build. Environ.* 149 (2019) 15–25. doi:10.1016/j.buildenv.2018.12.010.
- [11] D. Heinzerling, S. Schiavon, T. Webster, E. Arens, Indoor environmental quality assessment models: A literature review and a proposed weighting and classification scheme, *Build. Environ.* 70 (2013) 210–222. doi:10.1016/j.buildenv.2013.08.027.
- [12] H.H. Bruun, *Hot Wire Anemometry: Principles and Signal Analysis*, Oxford University Press, 1995.
- [13] Wikipedia, Anemometer, (n.d.). <https://en.wikipedia.org/wiki/Anemometer>.
- [14] TSI Inc, *VelociCalc Spec Sheet*, 2012. https://www.tsi.com/getmedia/945a561b-e714-4b80-8013-ac32654a91f0/9515-9535-9545-VelociCalc_US_2980569-web?ext=.pdf (accessed January 6, 2020).
- [15] Sensor Electronic, *SensoData5500*, (2018). <http://www.sensor-electronic.pl/>.
- [16] Kanomax, *Climomaster Anemometer Model 6501*, (2017). <https://www.kanomax-usa.com/product/climomaster-anemometer-model-6501-series/>.
- [17] A.K. Melikov, Z. Popiolek, M.C.G. Silva, I. Care, T. Sefker, Accuracy limitations for low-velocity measurements and draft assessment in rooms, *HVAC R Res.* 13 (2007) 971–986. doi:10.1080/10789669.2007.10391465.
- [18] TSI Inc, *TSI Thermal Anemometry Probes*, 2013. https://www.tsi.com/getmedia/2e3fafd5-8037-40a9-aa38-4fa05a1d3ef3/Hotwire_Catalog_2980465?ext=.pdf (accessed January 6, 2020).
- [19] R.J. Adamec, D.V. Thiel, Self heated thermo-resistive element hot wire anemometer, *IEEE Sens. J.* 10 (2010) 847–848. doi:10.1109/JSEN.2009.2035518.
- [20] Sonic Corporation, *Measurement of 3-Dimensional Wind Velocity Components*, 2018. <http://www.u-sonic.co.jp/english/pdf/em-WA-790.pdf>.
- [21] J.C. Kaimal, *Advances in Meteorology and the Evolution of Sonic Anemometry*, 2013. <http://www.apptech.com/wp-content/uploads/2016/08/Evolution-of-Sonic-Anemometry.pdf>.
- [22] J. Kochendorfer, T.P. Meyers, J.M. Frank, W.J. Massman, M.W. Heuer, Reply to the comment by Mauder on “How well can we measure the vertical wind speed? Implications for fluxes of energy and mass,” *Boundary-Layer Meteorol.* 147 (2013) 337–345. doi:10.1007/s10546-012-9792-8.
- [23] M. Mauder, M.J. Zeeman, Field intercomparison of prevailing sonic anemometers, *Atmos. Meas. Tech.* 11 (2018) 249–263. doi:10.5194/amt-11-249-2018.
- [24] T.W. Horst, S.R. Semmer, G. Maclean, Correction of a non-orthogonal, three-component sonic anemometer for flow distortion by transducer shadowing, *Boundary-Layer Meteorol.* 155 (2015) 371–395. doi:10.1007/s10546-015-0010-3.
- [25] J.M. Frank, W.J. Massman, E. Swiatek, H.A. Zimmerman, B.E. Ewers, J.M. Frank, W.J. Massman, E. Swiatek, H.A. Zimmerman, B.E. Ewers, All sonic anemometers need to correct for transducer and structural shadowing in their velocity measurements, *J. Atmos. Ocean. Technol.* 33 (2016) 149–167. doi:10.1175/JTECH-D-15-0171.1.
- [26] R.J. Przybyla, H.-Y. Tang, A. Guedes, S.E. Shelton, D.A. Horsley, B.E. Boser, 3D ultrasonic rangefinder on a chip, *IEEE J. Solid-State Circuits.* 50 (2015) 320–334. doi:10.1109/JSSC.2014.2364975.
- [27] R.J. Przybyla, S.E. Shelton, A. Guedes, I.I. Izyumin, M.H. Kline, D.A. Horsley, B.E. Boser, In-air rangefinding with an AlN piezoelectric micromachined ultrasound transducer, *IEEE Sens. J.* 11 (2011) 2690–2697. doi:10.1109/JSEN.2011.2157490.
- [28] H.-S. Kim, M.P. Andersen, K. Chen, S. Kumar, W.J. Zhao, K. Ma, D.E. Culler, System architecture directions for post-SoC/32-bit networked sensors, in: *Proc. 16th ACM Conf. Embed. Networked Sens. Syst. - SenSys '18*, ACM Press, New York, New York, USA, 2018: pp. 264–277. doi:10.1145/3274783.3274839.
- [29] A. Ghahramani, M. Zhu, R.J. Przybyla, M.P. Andersen, P. Galicia, T. Peffer, H. Zhang, E. Arens, Measuring air speed with a low-power MEMS ultrasonic anemometer via adaptive phase tracking,

- IEEE Sens. J. 99 (2019). doi:10.1109/JSEN.2019.2920648.
- [30] C. Yu, C. Guo, J. Liang, T. Wang, Ultrasonic wind velocity measurement based on phase discrimination technique, TELKOMNIKA Indones. J. Electr. Eng. 10 (2012). doi:10.11591/telkomnika.v10i6.1443.
- [31] D. Han, S. Kim, S. Park, Two-dimensional ultrasonic anemometer using the directivity angle of an ultrasonic sensor, Microelectronics J. 39 (2008) 1195–1199. doi:10.1016/J.MEJO.2008.01.090.
- [32] A.G. Yakunin, 3D Ultrasonic anemometer with tetrahedral arrangement of sensors, J. Phys. Conf. Ser. 881 012030 (2017) 1–7.
- [33] A. Wieser, F. Fiedler, U. Corsmeier, A. Wieser, F. Fiedler, U. Corsmeier, The influence of the sensor design on wind measurements with sonic anemometer systems, J. Atmos. Ocean. Technol. 18 (2001) 1585–1608. doi:10.1175/1520-0426(2001)018<1585:TIOTSD>2.0.CO;2.
- [34] U. Högström, A.-S. Smedman, Accuracy of sonic anemometers: laminar wind-tunnel calibrations compared to atmospheric in situ calibrations against a reference instrument, Boundary-Layer Meteorol. 111 (2004) 33–54. doi:10.1023/B:BOUN.0000011000.05248.47.
- [35] Omega, Laboratory Grade Benchtop Wind-Tunnel with Instrumentation | Omega Engineering, (2017). <https://www.omega.com/en-us/calibration-equipment/wind-tunnels/p/WT4401>.
- [36] R. M. Young Company, Ultrasonic Anemometer - Model 81000, (n.d.).